
1 **Interaction and quantum chemical analysis between sulfamethoxazole and copper on biochar**

2 Jinkui Zhong^{1,2*}, Jiawen He¹, Yixiang Bao³, Yin Zhang¹, Yuanhu Gao¹, Jing Li¹, Lin Liu¹

3 ¹ School of Environmental and Municipal Engineering, Lanzhou Jiaotong University, Lanzhou,
4 730070, China

5 ² Key laboratory of Yellow River Water Environment in Gansu Province, Lanzhou, 730070, China

6 ³ State Key Laboratory of Water Resource Protection and Utilization in Coal Mining, National
7 Institute of Clean and Low Carbon Energy, Beijing 102209, China

8 * Corresponding author: Jinkui Zhong

9 E-mail: zhongjk@mail.lzjtu.cn, tel: +86-13609343749

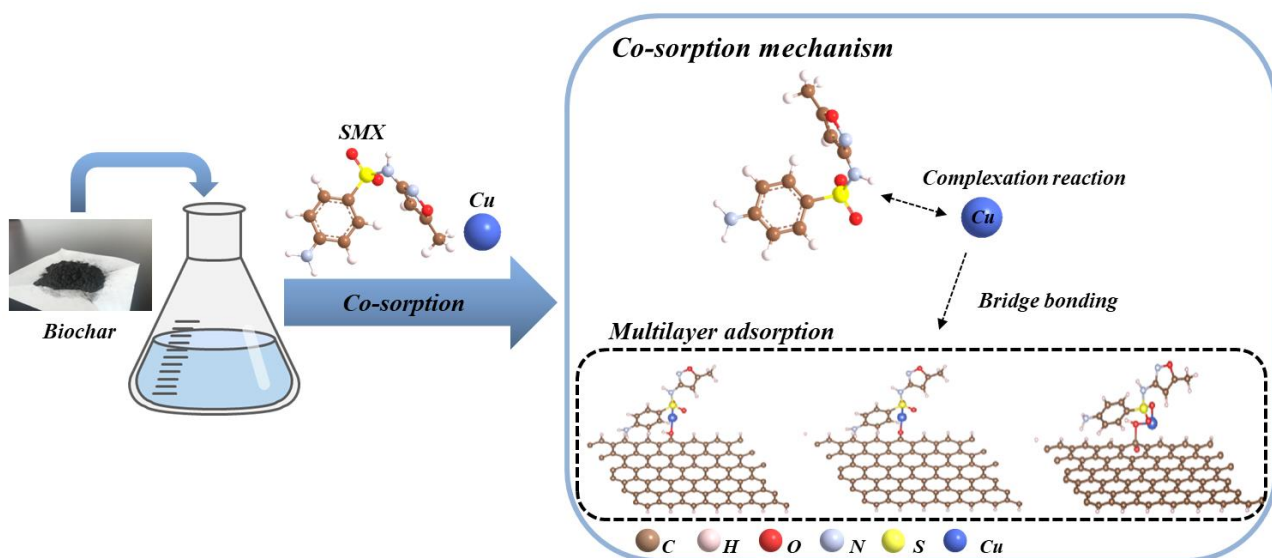
10 Other co-author E-mail: Jiawen He (1580054349@qq.com), Yixiang Bao (baoja2008@163.com),

11 Yin Zhang (yyinzzhang@163.com), Yuanhu Gao (2509458063@qq.com), Jing Li

12 (3122261970@qq.com), Lin Liu (2763970749@qq.com)

1

Graphical abstract



2

ACCEPTED MANUSCRIPT

1 **ABSTRACT**

2 Sulfamethoxazole (SMX) and copper (Cu) are common antibiotic and heavy metallic contaminants.
3 They can be removed separately through biochar sorption method. However, the interaction
4 between SMX and Cu remains an unresolved issue in the sorption process of biochar. In this paper,
5 two biochar samples were prepared from maize straw at temperatures of 300 °C and 600 °C. The
6 interaction between SMX and Cu in the sorption process on biochar was investigated using the
7 batch equilibrium experiment method and quantum chemical calculations. The results showed that
8 co-existing of SMX and Cu has a significant contribution to each other's sorption on biochar. In the
9 coexisting system of SMX and Cu, the sorption capacity of HBC600 for SMX and Cu were 24.22
10 mg/g and 96.23 mg/g, which were higher than the single system. Quantum chemical calculations
11 showed that due to the bridge bonding and complexation of Cu and SMX on the biochar, the
12 biochar may have formed OH-Cu-SMX, CO-Cu-SMX and COOH-Cu-SMX bonds with the
13 pollutants in the mixed system, and the sorption energy was significantly increased. This indicates
14 that the sorption capacity of biochar for both pollutants was enhanced in the mixed system.

15 **Keywords:** biochar, co-sorption, interaction, quantum chemical calculation

16 1. Introduction

17 The combined pollution from antibiotics and heavy metals (HMs) is attracting widespread attention
18 in recent years (Yao *et al.* 2020; Zhao *et al.* 2022). Sulfamethoxazole (SMX), a typical sulfonamide
19 antibiotic, which has been frequently observed in the surface water, groundwater and soil(Gao *et al.*
20 2014), is difficult to remove using classic wastewater treatment methods(Younes *et al.* 2019).
21 Numerous studies have demonstrated that the antibiotic not only stimulates the emergence of drug-
22 resistant bacteria, but also hampers the proliferation of microorganisms and plants, inflicting serious
23 damage on the ecological environment and human health (Han *et al.* 2020; Yao *et al.* 2012). Copper
24 (Cu), a common type of heavy metals, is widely used in industry and agriculture. Due to its non-
25 biodegradability and strong toxicity, Cu is one of the major heavy metal pollutants posing a serious
26 threat to the ecosystem and public health(Yan *et al.* 2010). The presence of antibiotics and heavy
27 metals can be detected in many water bodies and soils, and the combined coexistence of two
28 contaminants in the physical environment is frequently seen(Khurana *et al.* 2021; Shen *et al.* 2023a).
29 Co-existing contaminants of antibiotics and HMs have joint toxic effects on organisms such as
30 synergistic(Liu *et al.* 2021), antagonistic(Tong *et al.* 2015), or additive effects(You *et al.* 2022),
31 which complicate the impact on the environment(Shu *et al.* 2024[cited 2024 August 16];[71 p.]).
32 Moreover, As the interaction of functional groups on antibiotics with HMs ions (Cuprys *et al.* 2018;
33 Huang *et al.* 2017; Yang *et al.* 2022b), the combined contaminants are more difficult to remove
34 than the single contaminants(Li *et al.* 2018). For example, the amino functional groups and the N-
35 heteroaromatic rings of sulfamerazine maybe interact with Cu, and tend to form complexes,
36 weakening the reactivity of sulfamerazine molecules (Sha *et al.* 2022). Therefore, it is necessary to
37 explore the interaction mechanisms of combined contaminants of antibiotics and HMs on biochar to
38 find an effective treatment method for them.

39 Last years, various techniques, such as adsorption, biodegradation, and electrochemical methods,
40 have been developed and applied to combined pollution problems (Li *et al.* 2022; Liu *et al.* 2023;
41 Long *et al.* 2021). Of them, adsorption method is a low-cost, cost-effect and environmentally

42 friendly method for pollutants removal. A variety of materials can serve as adsorbents, including
43 carbon nanotube, alumina, activated carbon and biochar(Shan *et al.* 2015). Among these materials,
44 biochar, as an environmentally friendly material, has become a popular adsorbent for the removal of
45 organic and inorganic pollutants from polluted water due to its high porosity, large specific surface
46 area and rich functional groups (e.g. -COOH, -OH and C=O) that can be involved in sorption(Guo
47 *et al.* 2020). Currently, some researchers have conducted various studies to examine the
48 effectiveness and mechanisms of biochar in the individual adsorption of HMs or antibiotics(Hu *et al.*
49 2023; Pathy *et al.* 2023; Qiu *et al.* 2019; Truong *et al.* 2022). However, due to the complex
50 interaction mechanisms of combined pollutants that different antibiotic-HMs combined pollutants
51 may exhibit either promoting or inhibiting effects on the sorption behavior of different
52 materials(Deng *et al.* 2019; Wang *et al.* 2019; Yuan *et al.* 2019), reports on the effect of antibiotic-
53 HMs combined pollutants on the sorption behavior of biochar are still very limited. Therefore, in
54 this paper, a comparative study of the sorption of single and combined systems of antibiotics and
55 HMs was conducted to understand the sorption behavior and interaction of these contaminants
56 coexisting in biochar. SMX and Cu were selected as representatives of antibiotics and HMs,
57 respectively. Sorption experiments were carried out using the batch equilibrium experiment method
58 to determine the sorption data for single and combined pollutants of SMX and Cu by biochar. Based
59 on the experimental results, the quantum chemical calculation was performed. The formation
60 energies of the main chemical bonds on the biochar surface were calculated by first principles using
61 VASP (Vienna Ab initio Simulation Package) software. The sorption mechanisms and interaction
62 among biochar, SMX and Cu in the sorption process were explored which provides theoretical
63 support for the feasibility of removing antibiotic-HMs combined pollutants by biochar.

64 **2. Materials and methods**

65 *2.1. Sample preparation*

66 Sulfamethoxazole (SMX), purchased from Chongqing Cypress Technology Co., Ltd., was prepared
67 as a 100 mg/L stock solution with a background solution containing 0.01 mol/L NaNO₃ and 0.1%

68 NaN_3 , $\text{Cu}(\text{NO}_3)_2 \cdot 3\text{H}_2\text{O}$, obtained from Sinopharm Group Chemical Reagent Co., Ltd., was prepared
69 as a 1000 mg/L stock solution with deionized water. The pH was adjusted to 5 with 0.1 mol/L HCl
70 and 0.1 mol/L NaOH solution. All the chemicals were analytical reagents.

71 Maize straw, collected from a farmland in Gansu province, China, was chopped, passed through a
72 0.425 mm sieve, and converted to biochar by slow pyrolysis in a muffle furnace (SX2, Shanghai
73 Jiazhan Instrument Equipment Co., Ltd.) at 300 °C or 600 °C for 6 h in a nitrogen atmosphere. The
74 resultant biochar samples were abbreviated as BC300 and BC600. The biochar samples were then
75 crushed and sieved to obtain uniform 0.425 mm-sized particles. The biochar samples were washed
76 several times with 1 mol/L HCl and deionized water to remove ash until the pH value remained
77 constant. The resulting biochar samples were labeled HBC300 and HBC600. After the biochar
78 samples were dried at 80 °C for 12 h, they were stored in a sealed container for future use.

79 2.2. Characterization of the biochar

80 Total carbon (C), nitrogen (N), hydrogen (H), and sulfur (S) in the biochar were determined using
81 an elemental analyzer (Vario EL, a German element company). Oxygen content was determined by
82 mass balance (Kwak *et al.* 2019). Ash content was measured by heating the biochar samples at
83 $650 \pm 20^\circ\text{C}$ to a constant weight and calculated using equation (1). The yield of biochar was
84 calculated according to equation (2). Biochar functional groups were characterized using Fourier
85 transform infrared spectrometer (FTIR) (Nexus 870, Nicolet, USA). The specific surface area, total
86 pore volume, and pore size distribution of the biochars were measured using the nitrogen degassing
87 method (Alfaro Soto *et al.* 2019). The micromorphology features of biochar were observed by
88 scanning electron microscope (SEM) (JSM-5600LV, Japan Electron Optics).

$$89 \quad \text{ash} = \frac{m_2 - m_1}{m} \times 100\% \quad (1)$$

90 where m is the mass of the original biochar sample, g; m_1 is the mass of the empty crucible after
91 burning, g; m_2 is the mass of the crucible with biochar after ashing the original biochar at
92 $650 \pm 20^\circ\text{C}$ to constant weight and cooling, g.

$$\text{yield} = \frac{m_3 - m_1}{m_2 - m_1} \times 100\% \quad (2)$$

94 where m_1 is the mass of the crucible, g; m_2 is the mass of crucible with the powdered raw materials,
95 g; m_3 is the mass of the crucible containing the prepared biochar, g.

96 2.3 Experimental methods of sorption for SMX and Cu

97 Experiments were conducted in the laboratory of Gansu Province Wastewater Treatment Industry
98 Technology Center. At 298K, twenty-five milliliters of a certain concentration of SMX or Cu(II)
99 solution and a fixed mass of biochar (HBC300 or HBC600) were together added to a 50 mL
100 Erlenmeyer flask for sorption kinetic experiments by the batch equilibrium experiment method, in
101 which the sampling time was set from 0.1 to 24 h. The sorption isotherm experiments were divided
102 into two groups. In the first group, the initial concentration of fixed SMX was 50 mg/L, and the
103 concentration gradient of Cu(II) solution was 50-500 mg/L. In the second group, the initial
104 concentration of the fixed Cu(II) solution was 200 mg/L, and the SMX concentration gradient was
105 10-100 mg/L. Then these Erlenmeyer flasks were placed in a constant temperature shaker and
106 shaken at 150 rpm for 24 h. The suspension after shaking was filtered through a 0.45 μm filter
107 membrane for SMX and Cu analyses, where SMX was analyzed by High Performance Liquid
108 Chromatography (HPLC) and Cu was determined by flame atomic absorption spectrometry.

109 2.4 Kinetics sorption models

110 Quasi-first-order and quasi-second-order kinetic models are used to fit kinetic data as shown in
111 equations (3) and (4).

112 Quasi-first-order kinetic equation:

$$113 \quad Q_t = Q_e (1 - e^{-k_1 t}) \quad (3)$$

114 Quasi-second-order kinetic equation:

$$115 \quad Q_t = \frac{Q_e^2 k_2 t}{1 + Q_e k_2 t} \quad (4)$$

116 where Q_t is the amount of adsorbed substance at time t (h), mg/g; Q_e is the amount of adsorbed
117 substance at equilibrium, mg/g; k_1 (h^{-1}) and k_2 [$\text{g}/(\text{mg} \cdot \text{h})$] are the adsorption rate constants of quasi-
118 first-order and quasi-second-order kinetics, respectively.

119 2.5 Isotherm sorption models

120 Langmuir and Freundlich sorption equations are applied to fit the isothermal sorption data of the
121 adsorbates as shown in equations (5) and (6).

122 Langmuir equation:

$$123 \quad Q_e = \frac{Q_m K_L C_e}{1 + K_L C_e} \quad (5)$$

124 Freundlich equation:

$$125 \quad Q_e = K_F C_e^N \quad (6)$$

126 where Q_e is the amount of adsorbed substance at equilibrium, mg/g; C_e is the concentration of
127 adsorbate at equilibrium, mg/L; Q_m is the saturated sorption amount of adsorbate on the biochar;
128 K_L (L/mg), K_F ($(\text{L/g})^n$), and N are the constants of the equations.

129 2.6 Quantum chemical computational methods

130 In this study, the Vienna Ab initio Simulation Package (VASP) was used for all density functional
131 theory (DFT) calculations, and a generalized gradient approximation was applied to the Perdew-
132 Burke-Ernzerhof (PBE) functional equation. The projected augmented wave potentials were used to
133 describe the ion nuclei with a plane-wave basis set with a set-energy cut-off of 400 eV, the van der
134 Waals interactions were geometrically optimized using the DFT-D3 empirical corrections All
135 crystal structures were optimized with an energy convergence threshold of 1.0×10^{-5} eV for and
136 force convergence threshold of 0.03 eV/Å. To avoid interaction between two adjacent surfaces, the
137 vacuum spacing was set as 20.0 Å. and the sorption energies at each point are calculated according
138 to equations (7).

$$139 \quad E_{\text{ads}} = E_{\text{tot}}(\text{biochar+pollutant}) - E_{\text{suf}}(\text{biochar}) - E_{\text{tot}}(\text{pollutant}) \quad (7)$$

140 where E_{ads} is the sorption energy of the system, E_{tot} (biochar + pollutant) is the total energy of the
141 pollutant sorption system of the biochar, E_{suf} (biochar) is the total energy of the point of the biochar
142 surface, and E_{tot} (pollutant) is the energy of the pollutant at a single point.

143 3. Results and discussion

144 3.1 Characterization of biochar

145 Table 1 presents the physicochemical properties of biochar that has been synthesized at various
146 temperatures. With increasing pyrolysis temperatures, the yield of biochar decreases from 18.12%
147 of BC300 to 12.68% of BC600. This is mainly due to the original chemical bonds and biomass
148 interior materials, such as cellulose, hemicellulose, and lignin, being destroyed in the pyrolysis
149 process, generating volatile substances to escape and eventually causing the loss of biochar
150 mass(Schmidt *et al.* 2023). The ash content of the biochar has a positive correlation with the rise in
151 temperature. However, compared with BC300 and BC600, the ash content of HBC300 and
152 HBC600 is greatly reduced. This is attributed to the reaction between the carbonates and other
153 substances in the ash and H^+ during the acid washing process. The pH values of HBC300 and
154 HBC600 exhibit a smaller magnitude when compared to BC300 and BC600, owing to the alkaline
155 ions in the biochar react with H^+ in the acid wash solution. The presence of weak metal salts
156 (carbonates) in the ash of biochar is an important reason for the alkalinity of biochar(Yang *et al.*
157 2022a). The C content increases from 57.71% (BC300) to 63.42% (BC600), indicating that the
158 pyrolysis process of biomass is a carbon-rich process. The contents of O and H decrease with the
159 increase in pyrolysis temperature, proving that deoxygenation and dehydrogenation occur in the
160 pyrolysis of biomass(Mutsengerere *et al.* 2019). H/C is widely used to evaluate the aromatization
161 degree of biochar. The smaller the H/C, the higher the aromaticity and the stronger the stability of
162 biochar(Calvelo Pereira *et al.* 2011; Grutzmacher *et al.* 2018; Shen *et al.* 2023b). (N+O)/C is the
163 polarity value of biochar. The polarity increases with the rise of (N+O)/C. Therefore, as the
164 pyrolysis temperature increases, the aromaticity of the biochar increases, but the polarity decreases.

165

Table 1. Primary physicochemical parameters and elementary compositions of biochar

Samples	pH	Ash (%)	Element content (%)					Element ratio	
			C	H	N	O	S	(N+O)/C	H/C
BC300	9.64	16.9	57.71	2.85	1.01	21.27	0.26	0.39	0.05
BC600	10.6	23.4	63.42	1.24	1.13	10.45	0.36	0.18	0.02
HBC300	3.68	6.70	69.64	3.38	1.47	18.43	0.38	0.28	0.05
HBC600	3.62	7.04	77.70	1.77	1.51	11.50	0.48	0.17	0.02

166

167 Compared to BC300 and HBC300, the specific surface area (S_{BET}) of BC600 and HBC600
 168 increases significantly, by nearly 100 times, with increasing pyrolysis temperature (Table 2). This is
 169 probably due to the higher pyrolysis temperature, which cracks the biomass feedstock into volatiles
 170 that escape from the biochar and increase the pore structure of the biochar(Li *et al.* 2021).

171

Table 2. Porosity and BET surface areas of biochar

Adsorbent	¹ $S_{\text{BET}}(\text{m}^2/\text{g})$	² $S_{\text{t-plot}}(\text{m}^2/\text{g})$	³ $V_{\text{pore}}(\text{cm}^3/\text{g})$	⁴ $V_{\text{micro}}(\text{cm}^3/\text{g})$	⁵ A_{BET}
BC300	3.82	6.96×10^{-1}	6.75×10^{-3}	1.80×10^{-4}	7.06
BC600	3.16×10^2	2.20×10^2	1.59×10^{-1}	9.31×10^{-2}	2.01
HBC300	4.19	8.84×10^{-1}	5.52×10^{-3}	1.76×10^{-4}	5.26
HBC600	4.05×10^2	2.81×10^2	2.04×10^{-1}	1.19×10^{-1}	2.02

172

173

174

¹BET Specific surface area; ²t-plot Micro area; ³Single point total volume; ⁴t-pLot micropore volume; ⁵BET average pore size.

175

176

177

178

179

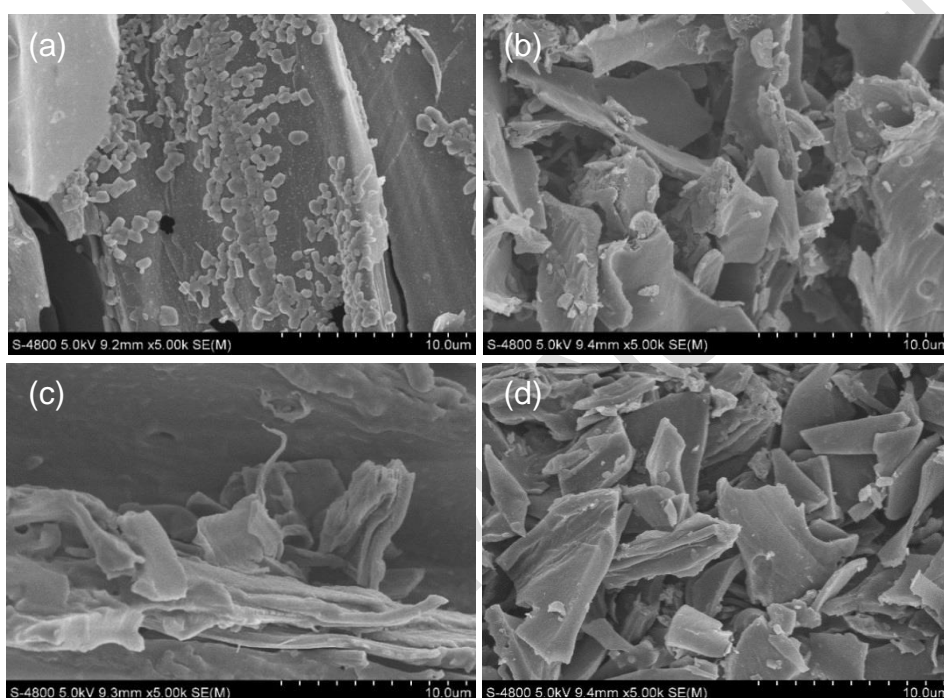
180

181

182

After acid washing, it is shown that the micropore area ($S_{\text{t-plot}}$) of HBC300 and HBC600 exhibits
 an increase. This rise suggests that the pore structure of biochar is blocked due to the presence of
 ash when the biochar is not subjected to acid washing. Following the acid washing process, most of
 the ash is removed from the biochar surface, and the pore structure on the biochar surface is
 exposed(Deng *et al.* 2023). When the pyrolysis temperature is 300 °C, the irregular lamellar
 structures of biochar remains relatively intact (Figure 1(a) and (c)). When the pyrolysis temperature
 reaches 600 °C, volatiles spill out of the pores due to further partitioning of the biomass to liberate
 large amounts of energy. As a result, a clearer pore structure can be observed (Figure 1(b) and (d)).

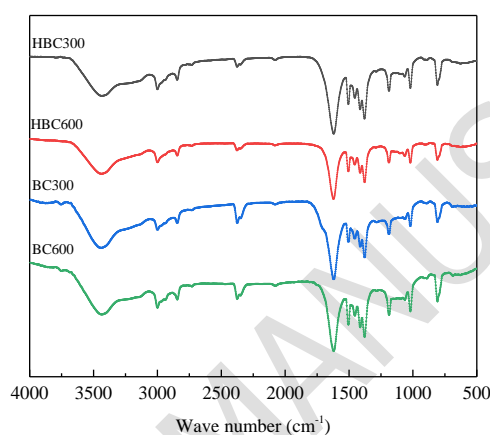
183 As the pyrolysis temperature increases, the pores in the biochar burst out, making the pores more
184 disorderly distributed, which is beneficial for improving the adsorption capacity of biochar.
185 Compared to the biochar before and after acid washing, the pore structures of HBC300 and
186 HBC600 are obviously exposed, the surface structures are clearer, and no excessive other debris or
187 impurities are present, which may be due to the ash and impurities in the biochar being washed
188 away by the acid solution (Figure 1(c) and (d)).



189
190 **Figure 1.** SEMs for BC300(a), BC600(b), HBC300(c), and HBC600(d)

191 The functional groups of biochar were characterized by FTIR. According to Figure 2, it can be
192 seen that BC300, BC600, HBC300, and HBC600 have the same characteristic peaks. The
193 absorption peak at 3421.46 cm^{-1} can be attributed to the stretching vibration of the hydroxyl
194 group (-OH). The appearance of the hydroxyl group is due to a large amount of cellulose and
195 hemicellulose in the biochar material is not destroyed at high temperatures. The absorbance peaks
196 at 2993.73 cm^{-1} and 2826.94 cm^{-1} indicate the presence of the saturated alkanes -CH₂ and -CH₃.
197 The peak at 2352.14 cm^{-1} may indicate the stretching vibration of C≡C or C=N. The peak at
198 1607.61 cm^{-1} is the C=C stretching vibration peak. The absorbance peaks between 1479.93 and
199 1375.32 cm^{-1} are mainly formed by the symmetric stretching of C=O in the carboxylate group

200 COO-. The C-O stretching (1159.14 cm^{-1}) occurs due to the presence of hydrocarbons, indicating
201 that hydroxyl and carboxyl groups may exist. The observed peaks at 978.79 cm^{-1} and 786.47 cm^{-1}
202 can be attributed to the deformation of Si-O-Si. It can be seen from Figure 2 that the positions of
203 the characteristic absorption peaks of biochar prepared from the same material are roughly the
204 same. However, there are variations in the values and widths of these absorption peaks,
205 suggesting that biochars produced from the same source material possess similar functional
206 groups, but the numbers are different(Anand *et al.* 2023; Keiluweit *et al.* 2010).



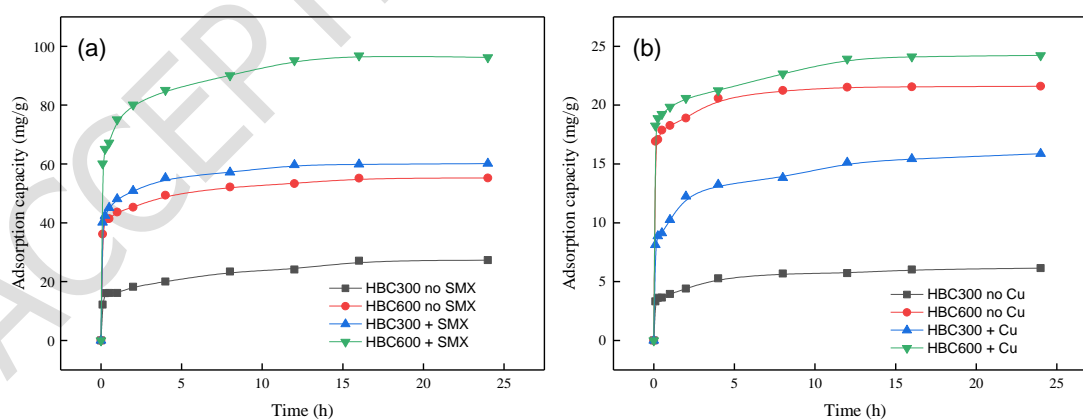
207
208 **Figure 2.** FTIR spectra for four types of biochar

209 3.2 Sorption kinetics

210 As shown in Figure 3, the amount of Cu/SMX adsorbed increases rapidly from 0 to 3 h, probably
211 due to the presence of a large number of adsorption sites on the surface of the biochar and the high
212 concentration of contaminants in the solution(Yan *et al.* 2020). With increasing adsorption time, the
213 adsorption rates slow down due to the limited number of adsorption sites on the biochar, and
214 eventually reach adsorption equilibrium at about 12 h. In the single system, the maximum
215 adsorption capacities of Cu on HBC300 and HBC600 are 27.35 and 55.23 mg/g, respectively
216 (Figure 3(a)). Similarly, it can be shown that the maximum adsorption capabilities for SMX are
217 6.14 and 21.61 mg/g on HBC300 and HBC600, respectively, as depicted in Figure 3(b). Obviously,
218 the adsorption capacities of biochar for Cu are higher than those for SMX. This may be due to the
219 fact that there exists a large number of negative charges on biochar that can continue to interact
220 with Cu(Wang and Liu 2017). Meanwhile, the adsorption capacities of HBC600 for SMX and Cu

221 are higher than those of HBC300. This may be due to the higher the pyrolysis temperature, the
222 greater the specific surface area of the biochar, and the stronger the adsorption for absorbates(Wang
223 *et al.* 2022).

224 Compared with the single system, the adsorption capacity of HBC300 and HBC600 for SMX and
225 Cu(II) in the mixed system increases to a certain extent. The maximum sorption of SMX and Cu(II)
226 by HBC600 in the mixed system reached 24.22 mg/g and 96.23 mg/g at 24h, which was higher than
227 the single sorption capacity of some modified biochar. For example, the maximum sorption of SMX
228 was only 14.73 mg/g for chitosan-biochar(Son Tran *et al.* 2023), and the maximum sorption of Cu
229 was only 38.6 mg/g for biochar loaded with MgAl-layered double hydroxide(Su *et al.* 2022).
230 Therefore, during the adsorption process, the synergistic effect between SMX and Cu(II) has an
231 important influence on the final adsorption capacity. The presence of Cu(II) can not only exchange
232 the cation in biochar, but also form a complex with SMX that are easily adsorbed by the biochar.
233 The complex has a strong affinity for biochar, resulting in enhanced adsorption of SMX and Cu(II)
234 on the biochar(Xu *et al.* 2023). In addition, π -electron interaction is emphasized for chemicals with
235 electron-donating. While the biochar adsorbs Cu(II), the SMX adsorbed on the biochar can also
236 combine with Cu(II) to further increase the adsorption capacity of Cu(II).



237
238 **Figure 3.** Effect of time on sorption of Cu(a) and SMX(b)

239 In order to study the adsorption rate in mixed system, quasi-first-order and quasi-second-order
240 kinetic equations were used to fit the kinetic data (Table 3). The equilibrium adsorption capacities,
241 Q_e , of the two pollutants in mixed system are higher than those in the single system, but there is a

242 certain increase in the difference in adsorption capacities due to the different adsorption orders of
 243 two different types of pollutants. The adsorption capacity of Cu increases greatly with the addition
 244 of SMX. The quasi-second-order rate constant, k_2 , in the mixed adsorption system increases greatly
 245 on HBC600 (from 0.46 to 1.24 g/(mg· h)) and HBC300 (from 0.32 to 0.97 g/(mg· h)). This may be
 246 due to, on the one hand, Cu(II) undergoes reactions, such as ion exchange and surface pore
 247 adsorption, on the surface of the biochar in the mixed system; on the other hand, Cu(II) complexes
 248 with SMX, forming the Cu(II)-SMX complex, which leads to a significant increase in the
 249 adsorption capacity(Yao *et al.* 2020).

250 As shown in Table 3, the R^2 values of the quasi-first-order kinetic model are lower than those of
 251 the quasi-second-order kinetic model. Moreover, the theory adsorption amounts of the quasi-
 252 second-order kinetic model are closer to the actual values, indicating that the quasi-second-order
 253 kinetic model is more suitable for describing the adsorption process of SMX and Cu(II) on biochar.
 254 The whole adsorption process includes the composite reaction of surface adsorption and intra-
 255 particle diffusion adsorption. Therefore, the quasi-second-order kinetic model can reflect the kinetic
 256 mechanism of this adsorption more comprehensively(Fang *et al.* 2014; Ho 2006). In addition, the
 257 adsorption rate constants of the mixed system are higher than those of the single system, indicating
 258 that the mixed system favors the adsorption efficiencies of biochar for SMX and Cu(II).

259 **Table 3.** Kinetic parameters of sorption of SMX and Cu(II) onto biochars

Pollutants	Biochar	quasi-first-order dynamics			quasi-second-order dynamics		
		Q_e (mg/g)	k_1 (h ⁻¹)	R^2	Q_e (mg/g)	k_2 (g/(mg· h))	R^2
SMX	HBC600 + Cu	18.07	0.50	0.8410	24.12	0.23	0.9715
	HBC600 no Cu	11.30	0.85	0.7496	19.60	0.13	0.9301
	HBC300 + Cu	12.34	0.02	0.8681	15.01	0.68	0.9017
	HBC300 no Cu	7.03	0.03	0.9177	6.29	0.48	0.9246
Cu (II)	HBC600 + SMX	70.12	0.42	0.8864	95.44	1.24	0.9821
	HBC600 no SMX	55.02	0.01	0.9118	60.34	0.46	0.9491
	HBC300 + SMX	48.70	0.51	0.9204	54.78	0.97	0.9120
	HBC300 no SMX	25.00	0.01	0.8573	27.01	0.32	0.9588

260

261 *3.3 Isothermal sorption*

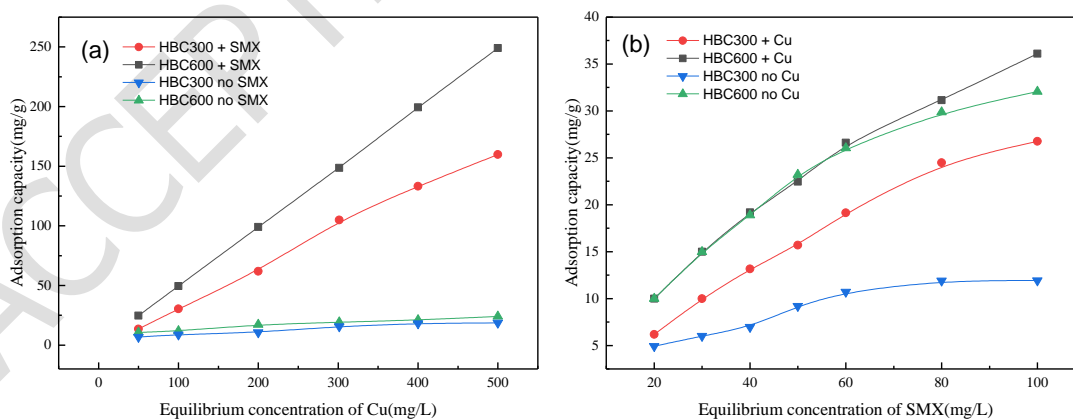
262 The adsorption isotherms of SMX and Cu are depicted in Figure 4, and the fitting parameters for
263 SMX and Cu are summarized in Table 4. As shown in Figure 4, the amount of SMX and Cu(II)
264 adsorbed by biochar increases with the equilibrium concentration. In the single system, due to the
265 large number of anions on the surface of biochar, Cu(II) ions undergo an adsorption reaction with
266 these anions through electrostatic attraction. At the same time, there are a large number of
267 functional groups on the surface of biochar, which allow heavy metals to precipitate or complex
268 with these functional groups. SMX molecules contain electron-poor parts (protonated amino
269 groups), so they can act as electron acceptors. The aromatic structure of biochar makes it a powerful
270 π electron donor, therefore functional groups have strong π -electron interactions with the aromatic
271 structure. Compared with the single system, adsorption capacity in the mixed system increased
272 significantly(Figure 4(a)). The maximum adsorption capacity of Cu on HBC300 increases from
273 18.74 mg/g in the single system to 159.80 mg/g in the mixed system. As for HBC600, the
274 maximum adsorption capacity of Cu increased from 24.01 mg/g in the single system to 249.05 mg/g
275 in the mixed system. Therefore, it is considered that Cu removal can be promoted when the SMX is
276 present. It could be because when the porous in the biochar are filled in by single Cu adsorption, the
277 sorption is difficult to continue. However, when SMX is added to the sorption system, -OH on the
278 biochar could combine with SMX to produce intermediates that sequentially coordinate with Cu(II).
279 In the same way, the amount of SMX adsorbed increases significantly with the presence of Cu. This
280 may be due to not only the pore adsorption and hydrogen bonding, but also that the adsorbed Cu(II)
281 on the biochar can act as a bridging bond for the adsorption of SMX. In addition, biochar also
282 contains rich carboxyl groups (-COOH), phenolic hydroxyl groups (-OH), and other oxygen-
283 containing functional groups that can form complexes with SMX and Cu(II). Langmuir and
284 Freundlich models were used to fit the isothermal data of SMX and Cu(II) adsorbed by biochar
285 (Table 4).

Table 4. Sorption isotherms parameters of SMX and Cu(II) onto biochar

Pollutants	Biochar	Langmuir			Freundlich		
		Q_m (mg/g)	K_L (L/mg)	R^2	K_F ((L/g) ⁿ)	$1/n$	R^2
SMX	HBC600 + Cu	35.07	0.50	0.8352	19.90	0.23	0.9706
	HBC600 no Cu	31.30	0.85	0.9310	19.60	0.13	0.9821
	HBC300 + Cu	25.34	0.02	0.9661	2.34	0.68	0.9785
	HBC300 no Cu	18.03	0.92	0.9247	1.59	0.48	0.9641
Cu(II)	HBC600 + SMX	240.12	0.42	0.9203	2.36	1.24	0.9516
	HBC600 no SMX	25.02	0.01	0.8619	1.12	0.46	0.9742
	HBC300 + SMX	164.70	0.51	0.9476	2.04	0.97	0.9599
	HBC300 no SMX	24.76	0.01	0.8858	1.23	0.32	0.9651

287

288 When the adsorption capacity of the adsorbent is strong, it can better conform to the Freundlich
 289 adsorption isotherm and deviate from the Langmuir isotherm. As the R^2 values of the Freundlich
 290 model range from 0.95 to 0.98 (Table 4), the Freundlich model fits better than the Langmuir model,
 291 indicating that the sorption of SMX and Cu on biochar is heterogeneous multilayer adsorption,
 292 including valence forces and van der Waals forces (Stromer *et al.* 2018). Judging from the
 293 parameters of the two sets of models, the adsorption capacity of the mixture system is enhanced.
 294 Therefore, it can be inferred that co-adsorption has a certain promotion effect on the removal of
 295 pollutants compared with single adsorption.



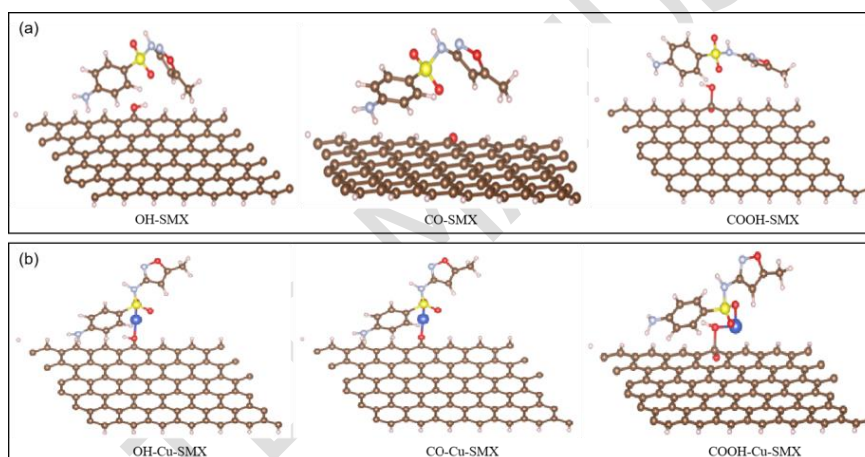
296

Figure 4. Sorption isotherms of Cu(II)(a) and SMX(b) on biochar

298 3.4 Quantum chemical calculation results

299 From the analysis of the kinetic and isothermal sorption, it can be seen that there may be OH-SMX
 300 bond, CO-SMX bond and COOH-SMX bond between biochar and SMX. Three kinds of O

301 containing functional groups on biochar including -OH, -CO and -COOH were considered as
302 adsorption sites for SMX and SMX-Cu complex. As shown in Table 5, Compared with -O and -
303 COOH, the sorption energy of SMX on -OH group of biochar is more negative, suggesting that -
304 OH group was the main sites for absorbing SMX. In addition, the sorption energies of OH-Cu-SMX
305 (-2.88 eV), CO-Cu-SMX (-3.12 eV), and COOH-Cu-SMX (-3.93 eV) formed by the simultaneous
306 sorption of SMX and Cu on the biochars were smaller than those of OH-SMX (-1.63 eV), CO-SMX
307 (-1.58 eV), and COOH-SMX bonds (-0.49 eV), indicating that the sorption of pollutants by biochar
308 is more favorable when two pollutants are co-existing. Moreover, for all -OH, -CO and -COOH
309 biochar configurations, the bond between Cu-SMX with biochar was clearly found (Figure 5). The
310 above results verified that Cu could act as bridge to enhance the adsorption of SMX on biochar.



311

312 **Figure 5.** Optimized configurations of sorption models for biochar in single(a) and mixed(b)
313 systems

314

315 **Table 5.** Total system energy and sorption energy for different binding units on biochar

	Calculation unit	Total system energy (eV)	sorption energy (eV)
pre-sorption	-OH	-829.51	-
	-CO	-826.12	-
	-COOH	-834.32	-
	-SMX	-177.46	-
	-Cu-SMX	-177.80	-
post-sorption	-OH-SMX	-1008.60	-1.63218923
	-CO-SMX	-1005.17	-1.58166821
	-COOH-SMX	-1012.27	-0.48921977
	-OH-Cu-SMX	-1010.19	-2.88216571
	-CO-Cu-SMX	-1007.04	-3.11984307
	-COOH-Cu-SMX	-1016.05	-3.93211981

316

317 **4 Conclusions**

318 This study examines the interaction between SMX and Cu on biochar. The results indicated that in
319 the mixed system, SMX and Cu have a synergistic effect on each other in the adsorption process of
320 maize straw biochar. When sorption equilibrium is reached, the optimum adsorption capacity of
321 HBC600 for Cu in the mixed system (96.23 mg/g) is much higher than that of the single system
322 (55.23 mg/g) in the mixed system. Similarly, the optimum adsorption capacity of HBC600 for SMX
323 is 24.22 mg/g in the mixed system, which is higher than that of the single system (21.61 mg/g).
324 Compared to the single system, the equilibrium adsorption capacities of HBC300 and HBC600 for
325 SMX and Cu(II) in the mixed system exhibited a notable increase, accompanied by a reduction in
326 the time required to attain adsorption equilibrium. This trend is consistent with the quasi-second-
327 order kinetic equation, indicating that the adsorbent has a strong sorption capacity in the mixed
328 system. In addition, the adsorption process was consistent with the Freundlich isotherm model,
329 indicating the multilayer heterogeneous sorption behavior of biochar in the mixed system.
330 According to the quantum chemical calculation results, OH-Cu-SMX, CO-Cu-SMX and COOH-
331 Cu-SMX bonds were formed on the biochar in the mixed system, and the sorption energies were

332 greater than those in the single system, indicating that it is more favorable for the sorption of the
333 two pollutants on the biochar in the mixed system.

334

335 **Acknowledgements**

336 All authors contributed to the study conception and design. We thank Yin Zhang, Yuanhu Gao, Jing
337 Li, and Lin Liu for material preparation, data collection, and analysis, Yixiang Bao for assistance
338 with computational analysis of quantum chemistry, Jiawen He for writing the manuscript, and
339 Jinkui Zhong for methodological, writing-review, and editorial guidance. All authors read and
340 approved the final manuscript.

341 **Funding**

342 This work was supported by National Natural Science Foundation of China (22366025), Plan
343 Project of Science and Technology of Gansu Province (20JR2RA002), Project of Innovation and
344 Entrepreneurship for Undergraduates in Lanzhou Jiaotong University (DC2410732CX0011)

345 **Declarations statement**

346 **Ethical Approval** Not applicable.

347 **Consent to Participate** Not applicable.

348 **Consent to Publish** Not applicable.

349 **Competing Interests** The authors declare no competing interests.

350

351 **References**

352 Alfaro Soto M.A., Lenhard R., Chang H.K. and van Genuchten M.T. (2019), Determination of
353 specific LNAPL volumes in soils having a multimodal pore-size distribution, *Journal of*
354 *Environmental Management*, **237**, 576-584.

355 Anand A., Gautam S. and Ram L.C. (2023), Feedstock and pyrolysis conditions affect suitability of
356 biochar for various sustainable energy and environmental applications, *Journal of Analytical*
357 *and Applied Pyrolysis*, **170**, 105881.

358 Calvelo Pereira R., Kaal J., Camps Arbestain M., Pardo Lorenzo R., Aitkenhead W., Hedley M.,
359 Macías F., Hindmarsh J. and Maciá-Agulló J.A. (2011), Contribution to characterisation of
360 biochar to estimate the labile fraction of carbon, *Organic Geochemistry*, **42**, 1331-1342.

361 Cuprys A., Pulicharla R., Lecka J., Brar S.K., Drogui P. and Surampalli R.Y. (2018), Ciprofloxacin-
362 metal complexes-stability and toxicity tests in the presence of humic substances, *Chemosphere*,
363 **202**, 549-559.

364 Deng L., Zhao Y., Sun S., Feng D. and Zhang W. (2023), Thermochemical method for controlling
365 pore structure to enhance hydrogen storage capacity of biochar, *International Journal of*
366 *Hydrogen Energy*, **48**, 21799-21813.

367 Deng R., Huang D., Zeng G., Wan J., Xue W., Wen X., Liu X., Chen S., Li J., Liu C. and Zhang Q.
368 (2019), Decontamination of lead and tetracycline from aqueous solution by a promising
369 carbonaceous nanocomposite: Interaction and mechanisms insight, *Bioresource Technology*,
370 **283**, 277-285.

371 Fang C., Zhang T., Li P., Jiang R.f. and Wang Y.c. (2014), Application of Magnesium Modified
372 Corn Biochar for Phosphorus Removal and Recovery from Swine Wastewater, *International*
373 *Journal of Environmental Research and Public Health*, **11**, 9217-9237.

374 Gao S., Zhao Z., Xu Y., Tian J., Qi H., Lin W. and Cui F. (2014), Oxidation of sulfamethoxazole
375 (SMX) by chlorine, ozone and permanganate-A comparative study, *Journal of Hazardous*
376 *Materials*, **274**, 258-269.

377 Grutzmacher P., Puga A.P., Bibar M.P.S., Coscione A.R., Packer A.P. and de Andrade C.A. (2018),
378 Carbon stability and mitigation of fertilizer induced N₂O emissions in soil amended with
379 biochar, *Science of The Total Environment*, **625**, 1459-1466.

380 Guo M., Song W. and Tian J. (2020), Biochar-Facilitated Soil Remediation: Mechanisms and
381 Efficacy Variations, *Frontiers in Environmental Science*, **8**, 521512.

382 Han Z., Zhang Y., An W., Lu J., Hu J. and Yang M. (2020), Antibiotic resistomes in drinking water
383 sources across a large geographical scale: Multiple drivers and co-occurrence with
384 opportunistic bacterial pathogens, *Water Research*, **183**, 116088.

385 Ho Y.S. (2006), Review of second-order models for adsorption systems, *Journal of Hazardous*
386 *Materials*, **136**, 681-689.

387 Hu T., Zhao S., Huang Y., Chen Z., Zhang X., Wei C., Zeng S. and Liu L. (2023), Potential
388 removals of tetracycline and sulfamethoxazole by iron-loaded sludge biochar, *Journal of Water*
389 *Process Engineering*, **54**, 103962.

390 Huang B., Liu Y., Li B., Liu S., Zeng G., Zeng Z., Wang X., Ning Q., Zheng B. and Yang C. (2017),
391 Effect of Cu(II) ions on the enhancement of tetracycline adsorption by Fe₃O₄@SiO₂-
392 Chitosan/graphene oxide nanocomposite, *Carbohydrate Polymers*, **157**, 576-585.

393 Keiluweit M., Nico P.S., Johnson M.G. and Kleber M. (2010), Dynamic Molecular Structure of
394 Plant Biomass-Derived Black Carbon (Biochar), *Environmental Science & Technology*, **44**,
395 1247-1253.

396 Khurana P., Pulicharla R. and Kaur Brar S. (2021), Antibiotic-metal complexes in wastewaters: fate
397 and treatment trajectory, *Environment International*, **157**, 106863.

398 Kwak J.H., Islam M.S., Wang S., Messele S.A., Naeth M.A., El Din M.G. and Chang S.X. (2019),
399 Biochar properties and lead(II) adsorption capacity depend on feedstock type, pyrolysis
400 temperature, and steam activation, *Chemosphere*, **231**, 393-404.

401 Li B., Xie X., Zhang L., Lin D., Wang S., Wang S., Xu H., Wang J., Huang Y., Zhang S. and Liu D.
402 (2021), Coke formation during rapid quenching of volatile vapors from fast pyrolysis of
403 cellulose, *Fuel*, **306**, 121658.

404 Li S., Hu S., Jiang W., Liu Y., Zhou Y., Liu Y. and Mo L. (2018), Hierarchical architectures of
405 bismuth molybdate nanosheets onto nickel titanate nanofibers: Facile synthesis and efficient
406 photocatalytic removal of tetracycline hydrochloride, *Journal of Colloid and Interface Science*,
407 **521**, 42-49.

408 Li Y., Wu M., Wu J., Wang Y., Zheng Z. and Jiang Z. (2022), Mechanistic insight and rapid co-
409 adsorption of nitrogen pollution from micro-polluted water over MgAl-layered double
410 hydroxide composite based on zeolite, *Separation and Purification Technology*, **297**, 121484.

411 Liu L., Si L., Yang J., Peng L., Qiao S., Sun Y. and Guo C. (2023), Biodegradation and process
412 optimization of phenol and formaldehyde by *Aspergillus nomius* SGFA1, *International*
413 *Biodeterioration & Biodegradation*, **182**, 105630.

414 Liu X., Shao Y., Dong Y., Dong M., Xu Z., Hu X. and Liu A. (2021), Response of ammonia-
415 oxidizing archaea and bacteria to sulfadiazine and copper and their interaction in black soils,
416 *Environmental Science and Pollution Research*, **28**, 11357-11368.

417 Long L.L., Bai C.w., Zhang S.R., Deng S.H., Zhang Y.Z., He J.S., Wu J., Chen C. and Yang G.
418 (2021), Staged and efficient removal of tetracycline and Cu²⁺ combined pollution: A designed
419 double-chamber electrochemistry system using 3D rGO, *Journal of Cleaner Production*, **305**,
420 127101.

421 Mutsengerere S., Chihobo C.H., Musadamba D. and Nhapi I. (2019), A review of operating
422 parameters affecting bio-oil yield in microwave pyrolysis of lignocellulosic biomass,
423 *Renewable and Sustainable Energy Reviews*, **104**, 328-336.

424 Pathy A., Pokharel P., Chen X., Balasubramanian P. and Chang S.X. (2023), Activation methods
425 increase biochar's potential for heavy-metal adsorption and environmental remediation: A
426 global meta-analysis, *Science of The Total Environment*, **865**, 161252.

427 Qiu L.Q., Zhang L., Tang K., Chen G., Kumar Khanal S. and Lu H. (2019), Removal of
428 sulfamethoxazole (SMX) in sulfate-reducing flocculent and granular sludge systems,
429 *Bioresource Technology*, **288**, 121592.

430 Schmidt M.P., Ashworth D.J., Celis N. and Ibekwe A.M. (2023), Optimizing date palm leaf and
431 pistachio shell biochar properties for antibiotic adsorption by varying pyrolysis temperature,
432 *Bioresource Technology Reports*, **21**, 101325.

- 433 Sha J., Li L., An Z., He M., Yu H., Wang Y., Gao B. and Xu S. (2022), Diametrically opposite
434 effect of Cu^{2+} on sulfamerazine and ciprofloxacin adsorption-photodegradation in g-
435 C_3N_4 /visible light system: behavior and mechanism study, *Chemical Engineering Journal*, **428**,
436 131065.
- 437 Shan J., Ji R., Yu Y., Xie Z. and Yan X. (2015), Biochar, activated carbon and carbon nanotubes
438 have different effects on fate of ^{14}C -catechol and microbial community in soil, *Scientific*
439 *Reports*, **5**, 16000.
- 440 Shen C., He M., Zhang J., Liu J., Su J. and Dai J. (2023a), Effects of the coexistence of antibiotics
441 and heavy metals on the fate of antibiotic resistance genes in chicken manure and surrounding
442 soils, *Ecotoxicology and Environmental Safety*, **263**, 115367.
- 443 Shen J., Wu Y., Lan G., Xia Y., Yan B., Li Y., Zhang Y., Yu Y., Fu C., Xu A., Zhou J., Zhu A.
444 and Chen D. (2023b), Effect of co-pyrolysis of sewage sludge with different plastics on the
445 nitrogen, sulfur, and chlorine releasing characteristics and the heavy metals ecological risk of
446 biochar, *Journal of Environmental Chemical Engineering*, **11**, 110406.
- 447 Shu Y., Li D., Xie T., Zhao K., Zhou L. and Li F. (2024[cited 2024 August 16];[71 p.]), Antibiotics-
448 heavy metals combined pollution in agricultural soils: Sources, fate, risks, and
449 countermeasures, *Green Energy & Environment*.
- 450 Son Tran V., Hao Ngo H., Guo W., Ha Nguyen T., Mai Ly Luong T., Huan Nguyen X., Lan Anh
451 Phan T., Trong Le V., Phuong Nguyen M. and Khai Nguyen M. (2023), New chitosan-biochar
452 composite derived from agricultural waste for removing sulfamethoxazole antibiotics in water,
453 *Bioresource Technology*, **385**, 129384.
- 454 Stromer B.S., Woodbury B. and Williams C.F. (2018), Tylosin sorption to diatomaceous earth
455 described by Langmuir isotherm and Freundlich isotherm models, *Chemosphere*, **193**, 912-920.
- 456 Su X., Chen Y., Li Y., Li J., Song W., Li X. and Yan L. (2022), Enhanced adsorption of aqueous
457 Pb(II) and Cu(II) by biochar loaded with layered double hydroxide: Crucial role of mineral
458 precipitation, *Journal of Molecular Liquids*, **357**, 119083.

- 459 Tong F., Zhao Y., Gu X., Gu C. and Lee C.C.C. (2015), Joint toxicity of tetracycline with copper(II)
460 and cadmium(II) to *Vibrio fischeri*: effect of complexation reaction, *Ecotoxicology*, **24**, 346-
461 355.
- 462 Truong Q.M., Ho P.N.T., Nguyen T.B., Chen W.H., Bui X.T., Kumar Patel A., Rani Singhanian R.,
463 Chen C.W. and Dong C.D. (2022), Magnetic biochar derived from macroalgal *Sargassum*
464 *hemiphyllum* for highly efficient adsorption of Cu(II): Influencing factors and reusability,
465 *Bioresource Technology*, **361**, 127732.
- 466 Wang W., Kang R., Yin Y., Tu S. and Ye L. (2022), Two-step pyrolysis biochar derived from agro-
467 waste for antibiotics removal: Mechanisms and stability, *Chemosphere*, **292**, 133454.
- 468 Wang Y. and Liu R. (2017), Comparison of characteristics of twenty-one types of biochar and their
469 ability to remove multi-heavy metals and methylene blue in solution, *Fuel Processing*
470 *Technology*, **160**, 55-63.
- 471 Wang Y., Wang X., Li J., Li Y., Xia S., Zhao J., Minale T.M. and Gu Z. (2019), Co-adsorption of
472 tetracycline and copper(II) onto struvite loaded zeolite - An environmentally friendly product
473 recovered from swine biogas slurry, *Chemical Engineering Journal*, **371**, 366-377.
- 474 Xu Z., Huang W., Wang S., Song H., Xu J., Mailhot G., Tong Z., Zhang H. and Li Z. (2023), Co-
475 adsorption characteristics of antibiotics with different functional groups and cadmium
476 combined contamination on activated carbon, *Journal of Environmental Chemical Engineering*,
477 **11**, 110070.
- 478 Yan L., Liu Y., Zhang Y., Liu S., Wang C., Chen W., Liu C., Chen Z. and Zhang Y. (2020), ZnCl₂
479 modified biochar derived from aerobic granular sludge for developed microporosity and
480 enhanced adsorption to tetracycline, *Bioresource Technology*, **297**, 122381.
- 481 Yan S., Subramanian S.B., Tyagi R.D., Surampalli Rao Y. and Zhang Tian C. (2010), Emerging
482 Contaminants of Environmental Concern: Source, Transport, Fate, and Treatment, *Practice*
483 *Periodical of Hazardous, Toxic, and Radioactive Waste Management*, **14**, 2-20.

484 Yang S., Zhang L. and Duan F. (2022a), Effects of acid pickling and nitrogen doping on the biochar-
485 NO reaction performance of different biochars under high O₂ conditions, *Journal of the Energy*
486 *Institute*, **103**, 128-137.

487 Yang Y., Luo X., Zhang J., Ma X., Sun P. and Zhao L. (2022b), Sewage sludge-coconut fiber co-
488 pyrolysis biochar: Mechanisms underlying synergistic heavy metal stabilization and
489 ciprofloxacin adsorption, *Journal of Cleaner Production*, **375**, 134149.

490 Yao N., Li C., Yu J., Xu Q., Wei S., Tian Z., Yang Z., Yang W. and Shen J. (2020), Insight into
491 adsorption of combined antibiotic-heavy metal contaminants on graphene oxide in water,
492 *Separation and Purification Technology*, **236**, 116278.

493 Yao Y., Gao B., Chen H., Jiang L., Inyang M., Zimmerman A.R., Cao X., Yang L., Xue Y. and Li H.
494 (2012), Adsorption of sulfamethoxazole on biochar and its impact on reclaimed water
495 irrigation, *Journal of Hazardous Materials*, **209-210**, 408-413.

496 You X., Li H., Pan B., You M. and Sun W. (2022), Interactions between antibiotics and heavy
497 metals determine their combined toxicity to *Synechocystis* sp, *Journal of Hazardous Materials*,
498 **424**, 127707.

499 Younes H.A., Mahmoud H.M., Abdelrahman M.M. and Nassar H.F. (2019), Seasonal occurrence,
500 removal efficiency and associated ecological risk assessment of three antibiotics in a municipal
501 wastewater treatment plant in Egypt, *Environmental Nanotechnology, Monitoring &*
502 *Management*, **12**, 100239.

503 Yuan L., Yan M., Huang Z., He K., Zeng G., Chen A., Hu L., Li H., Peng M., Huang T. and Chen G.
504 (2019), Influences of pH and metal ions on the interactions of oxytetracycline onto nano-
505 hydroxyapatite and their co-adsorption behavior in aqueous solution, *Journal of Colloid and*
506 *Interface Science*, **541**, 101-113.

507 Zhao R., Ding W., Sun M., Yang L., Liu B., Zheng H. and Li H. (2022), Insight into the co-removal
508 of Cu(II) and ciprofloxacin by calcite-biochar composite: Enhancement and competition,
509 *Separation and Purification Technology*, **287**, 120487.

ACCEPTED MANUSCRIPT